

Improved decohesion modeling with the material point method for simulating crack evolution

Pengfei Yang · Yong Gan · Xiong Zhang ·
Zhen Chen · Wanjun Qi · Ping Liu

Received: 29 August 2013 / Accepted: 18 December 2013
© Springer Science+Business Media Dordrecht 2014

Abstract A combined elastoplasticity and decohesion model is used with the material point method for the crack problem as described in the Sandia National Laboratories challenge. To predict the cracking path in a complex configuration with the least computational cost, the decohesion modeling is improved by making the failure mode adjustable and by replacing the critical normal and tangential decohesion strengths with the tensile and shear peak strengths, without performing discontinuous bifurcation analysis in each loading step after the onset of failure is identified. It is found that there is a transition between different failure modes along the cracking path, which depends on the stress distribution around the path due to the nonlocal nature of failure evolution. Based on the parametric study and available experimental data, the proposed model-based

simulation procedure could be calibrated to predict the essential feature of the observed cracking response.

Keywords Material point method · Decohesion model · Crack evolution

1 Introduction

Two different kinds of approaches are available for modeling and simulating the evolution of localized material failure, namely, continuous and discontinuous ones. Decohesion and fracture mechanics models are representative of discontinuous approaches, in which strong discontinuities are introduced into a continuum body such that the governing differential equation is well-posed for given boundary and/or initial data. On the other hand, nonlocal (integral or strain gradient) models, Cosserat continuum models and rate-dependent models are among the continuous approaches proposed to regularize the localization problems, in which the higher order terms in space and/or time are introduced into the constitutive models so that the governing equations remain well-posed in a higher order sense for given boundary and/or initial data. Usually, only weak discontinuities in the kinematical field variables are allowed in the continuous approaches; i.e., the continuity of displacement field must hold in the continuum during the failure evolution. There exist certain kinds of applicability and limitation for different approaches, depending on the scale of the

P. Yang · X. Zhang (✉) · P. Liu
Department of Engineering Mechanics, Tsinghua
University, Beijing 100084, China
e-mail: xzhang@tsinghua.edu.cn

Y. Gan · W. Qi
Department of Engineering Mechanics, Zhejiang
University, Hangzhou 310027, China

Z. Chen (✉)
Department of Civil and Environmental Engineering,
University of Missouri, Columbia, MO 65211, USA
e-mail: chenzh@missouri.edu

Z. Chen
Department of Engineering Mechanics, Dalian University
of Technology, Dalian 116024, China

problem and the degrees of discontinuity considered (Bazant and Chen 1997).

If a continuous approach is considered, the use of higher order terms in space makes it difficult to perform large-scale computer simulation, due to the limitation of current computational capabilities. As shown in the previous research (Chen and Sulsky 1995), however, the evolution of localization might be equally well characterized by the formation and propagation of a moving material surface of discontinuity. An attempt has been made to investigate the use of the jump forms of conservation laws in defining the moving material surface (Chen 1996). By taking the initial point of localization as that point where the type of the governing differential equation changes, a moving material surface of discontinuity can be defined through the jump forms of conservation laws across the surface. Because the type change from a hyperbolic equation to an elliptic one could be represented by a parabolic (diffusion) one, both analytical and numerical solutions have been obtained to model the evolution of localization as damage diffusion, without invoking the use of higher order terms in constitutive modeling (Chen et al. 2002; among others). Since the essential feature of a complete failure evolution process is characterized by the transition between discontinuities of different degrees, the discontinuous bifurcation analysis could be employed to identify the transition from continuous to discontinuous failure modes (Chen et al. 2005; among others). To catch the essential feature of crack evolution, as described in the Sandia National Laboratories (SNL) challenge, with sound theoretical foundation and low computational cost, a local elastoplasticity model could be combined with the evolution of decohesion via the discontinuous bifurcation analysis for constitutive modeling, based on the previous work (Chen et al. 2005). As a result, all the model parameters could be calibrated based on the available experimental data. To predict a reasonable cracking path in a complicated configuration with the least computational cost, however, the existing decohesion modeling must be improved with an effective spatial discretization scheme.

Over the last two decades, much research has been conducted to circumvent the difficulty associated with the mesh-based methods, such as the finite element method (FEM) and finite difference method (FDM), in spatial discretization of crack propagation. As indicated by Belytschko et al. (1996), the meshless (mesh-

free) methods are uniquely suitable for those problems for which the conventional mesh-based methods are handicapped. The key difference among different spatial discretization methods is how the gradient and divergence terms are calculated. Because the meshless methods do not use a rigid mesh connectivity as compared with the FEM and FDM, the interpolation in the moving domain of influence is the common feature of the meshless methods.

The material point method (MPM) is an extension to solid dynamics problems of a hydrodynamics code called FLIP, which, in turn, evolved from the Particle-in-Cell Method. The motivation of the initial development was to simulate those challenging problems for which the FEM is limited, such as impact/contact, penetration and perforation with history-dependent internal state variables (Sulsky et al. 1994; among others). The essential idea is to take advantage of both the Eulerian and Lagrangian methods while avoiding the shortcomings of each. In comparison with the other recently developed numerical methods, the MPM appears to be less complex with a cost factor of at most twice that associated with the use of corresponding finite elements (Chen et al. 2002). Based on the MPM, a computer test-bed has been developed to integrate three basic types of governing differential equations (hyperbolic, parabolic and elliptic ones) into a single computational domain to perform the first-principle simulation of impact/blast-resistant structural responses (Chen et al. 2003, 2008; Hu and Chen 2006; Shen and Chen 2005; Zhang et al. 2009; Huang et al. 2011; Yang et al. 2012; among others). On the other hand, both the MPM and Peridynamics (Silling 2000; Silling et al. 2003; Silling and Askari 2005) could be classified as the particle-based methods without a rigid mesh connectivity, but the motivations for developing these two methods and associated approaches are different. The MPM has been developed to simulate multi-phase interactions involving failure evolution by using single-valued mapping and remapping between material points and background grid nodes, while the Peridynamics has been developed to handle discontinuities in a single-phase material, such as crack propagation, by formulating the integral equations over the domain of influence. Thus, the computational cost with the MPM for the SNL challenge would be higher than that with the Peridynamics. However, the main objective of the present study is to examine the capability for the MPM to discretize complex cracking paths in order to find

out how to improve the MPM for better dealing with multi-phase interactions involving crack propagation.

In the remaining of the paper, the improved constitutive model is described and implemented into MPM3D (Ma et al. 2010), a three-dimensional explicit MPM code (serial version), to tackle the SNL challenge with the least computational cost. It should be noted that the MPM has not been applied to the complex cracking problem as stated in the SNL challenge although it has been developed to simulate the simple types of fracture (Nairn 2003).

2 Improved decohesion modeling

In the MPM simulations, the material behavior is initially described by the von Mises associated elastoplasticity (a local model), and the decohesion model is then employed after the onset of failure is identified via the discontinuous bifurcation analysis based on the previous work (Chen et al. 2005). Since the continuum tangent stiffness tensor formulated from the associated von Mises model is symmetric, the peak strength coincides with the onset of discontinuous bifurcation. It is assumed that no plasticity occurs once decohesion has started so that the decohesion model replaces strain softening in the local elastoplasticity model to avoid the extra computational cost if a nonlocal stain softening model is invoked. Since the decohesion model predicts mode I, II or mixed mode failure, the failure patterns predicted by a nonlocal von Mises softening model are excluded. The decohesion model consists of the following equations:

$$\dot{\sigma} = E : (\dot{\epsilon} - \dot{\epsilon}^d) \tag{1}$$

$$\dot{\tau} = \dot{\sigma} \cdot n \tag{2}$$

$$\dot{u}^d = \dot{\lambda}^d \cdot m \tag{3}$$

$$\dot{\epsilon}^d = \frac{1}{2L_e} (n \otimes \dot{u}^d + \dot{u}^d \otimes n) \tag{4}$$

$$F^d = \tau^e - U_0 [1 - (\lambda^d)^q] = 0 \tag{5}$$

where ϵ^d is the decohesion strain tensor with the assumption of no plastic strain increase during the decohesion evolution so that the rate of change in stress is equal to the rate of change in elastic strain as shown in Eq. (1), λ^d is a dimensionless monotonically increasing variable for parameterizing the development of the decohesion, τ is the traction vector on the decohesion surface with the normal n , the effective length L_e is the ratio of the element volume to the decohesion surface

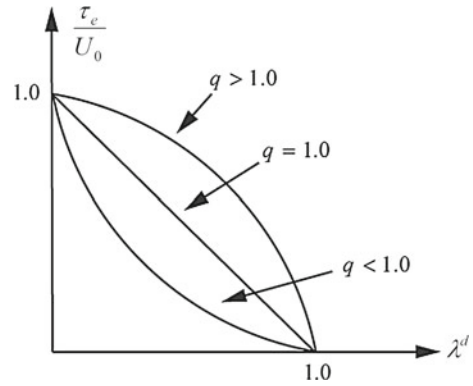


Fig. 1 Normalized relation between the effective traction and decohesion

area within the material point (element), u^d is the decohesion vector used to determine the decohesion strain, U_0 is the reference surface energy equal to the product of the reference decohesion \bar{u}_0 and the reference traction $\bar{\tau}_0$, and F^d is the flow surface for the decohesion evolution. The normalized relation between the effective traction τ^e and effective decohesion λ^d is adjusted by parameter q , as depicted in Fig. 1. For purpose of simplicity, the evolution function of decohesion is chosen to be associated, namely,

$$m = \bar{u}_0 \frac{A_d \cdot \tau}{(\tau \cdot A_d \cdot \tau)^{1/2}} \tag{6}$$

The effective traction τ^e is then computed as

$$\tau^e = \tau \cdot m = \bar{u}_0 (\tau \cdot A_d \cdot \tau)^{1/2} \tag{7}$$

The positive definite tensor of material parameters, A_d , is expressed by

$$[A_d] = \bar{\tau}_0^2 \begin{bmatrix} \frac{1}{\tau_{nf}^2} & 0 \\ 0 & \frac{1}{\tau_{tf}^2} \end{bmatrix} \tag{8}$$

with τ_{nf} and τ_{tf} denoting the failure initiation values for the Mode I and Mode II cases, respectively. At the beginning of decohesion, the consistency condition derived from Eq. (5) yields $\tau^e = U_0 = \bar{u}_0 \bar{\tau}_0$ with τ^e having the dimension of surface energy and $\bar{\tau}_0$ the dimension of stress, respectively. As a result, it follows that

$$\frac{\tau_n^2}{\tau_{nf}^2} + \frac{\tau_t^2}{\tau_{tf}^2} = 1 \tag{9}$$

where τ_n and τ_t are the normal and tangential stress components on the failure surface, respectively. By

introducing $c_m = \frac{\tau_{nf}}{\tau_t}$, τ_{nf} and τ_t are related to the given value of c_m . As can be seen from Eq. (9), different values of c_m would result in various failure modes. For example, $c_m = 100$ can be used for mode I failure, 0.01 for mode II failure, and 1.0 for mix mode failure. Let s_1, s_2 and s_3 represent the principal stresses in the order of magnitude. Then, we set $\tau_t = (s_1 - s_3)/(s_1 - s_3) / 2$ and $\tau_n = s_1$. It can be found at the onset of decohesion that

$$\tau_{nf} = \sqrt{s_1^2 + \frac{(s_1 - s_3)^2}{4c_m^2}} \tag{10}$$

Hence, τ_{nf} as determined from Eq. (10) could be used in Eq. (9) to find the effective traction during the evolution of decohesion for a given failure mode (c_m). To reduce the computational cost, the discontinuous bifurcation criterion is replaced with the limit strength criterion to identify the onset of decohesion because both criteria coincide with each other for the associated von Mises elastoplasticity model. As a result, the decohesion model is active based on the following criteria, with s_{max} and τ_{max} defined respectively as the tensile and shear strengths of the material:

- (1) mode I failure occurs if $s_1 > s_{max}$ only,
- (2) mode II failure occurs if $\tau_t > \tau_{max}$ only, and
- (3) mode I & II mixed failure occurs if both $s_1 > s_{max}$ and $\tau_t > \tau_{max}$ are satisfied.

With the unit vectors along the principal directions being $\mathbf{n}_1, \mathbf{n}_2$ and \mathbf{n}_3 for s_1, s_2 and s_3 , respectively, the normal vectors of the decohesion surface, \mathbf{n} , for the above three failure modes are given as

$$\mathbf{n} = \mathbf{n}_1 \quad (\text{mode I}) \tag{11}$$

$$\mathbf{n} = \frac{\mathbf{n}_2 \times (\mathbf{n}_1 + \mathbf{n}_3)}{|\mathbf{n}_2 \times (\mathbf{n}_1 + \mathbf{n}_3)|} \quad (\text{mode II}) \tag{12}$$

$$\mathbf{n} = \frac{\bar{\mathbf{n}}}{|\bar{\mathbf{n}}|}, \bar{\mathbf{n}} = \mathbf{n}_1 + \frac{\mathbf{n}_2 \times (\mathbf{n}_1 + \mathbf{n}_3)}{|\mathbf{n}_2 \times (\mathbf{n}_1 + \mathbf{n}_3)|} \quad (\text{mixed mode}) \tag{13}$$

Based on the consistency condition, a one-step algorithm can be designed by taking a Taylor series expansion of F^d about the trial state to the order of $(\Delta\lambda^d)^2$, namely

$$F^d = \frac{\partial F^d}{\partial \lambda} \Big|_{tr} \Delta\lambda^d + \left\{ \tau^e - U_0 \left[1 - (\lambda^d)^q \right] \right\} \Big|_{tr} + O\left(\Delta\lambda^d\right)^2 = 0 \tag{14}$$

With the given local strain increments at each material point and at each time step, it is assumed that no decohesion occurs in the beginning of the time step in order to get the trial stresses and traction through Eqs. (1) and (2). The value of F^d can then be determined based on the trial state and existing value of λ^d . If $F^d \leq tol$ with tol being a small positive number, the step is elastic without further decohesion. Otherwise, $\Delta\lambda^d$ is obtained from Eq. (14), and the decohesion strain tensor $\boldsymbol{\epsilon}^d$ is updated at the end of the time step by Eqs. (3) and (4) with the effective length L_e defined as $L_e = hm_1 + hm_2 + hm_3$ with $\mathbf{m} = m_1\mathbf{e}_1 + m_2\mathbf{e}_2 + m_3\mathbf{e}_3$, and h being the cell size of the background grid in the MPM.

3 Parametric study and demonstration

3.1 Uniaxial tension

Sandia National Laboratories chose the metal alloy with the density $\rho = 7.81 \times 10^{-3} \text{ g/mm}^3$, Poisson's ratio $\nu = 0.3$, elasticity modulus $E = 195 \text{ GPa}$ and the yield strength $\sigma_y = 1,100 \text{ MPa}$. In the simulations, the von Mises elastoplasticity model with linear strain hardening is used before decohesion occurs. The hardening modulus E_T is determined by the uniaxial tension test, for which the specimen geometry is given in Fig. 3 of the lead article. In the experiment, the loading rate is 0.0127 mm/s. In the MPM simulation, however, the actual loading rate would result in a large computational cost due to the explicit time integration algorithm implemented in MPM3D (Ma et al. 2010) to be used in this study. Figure 2 plots the engineering stress–engineering strain ($\sigma - \epsilon$) curve for $E_T = 1,150 \text{ MPa}$. The legend *ep_{ef}* in the figure represents the equivalent plastic strain. The effect of loading velocity v used in the simulation is also demonstrated in Fig. 2. It can be found that when v becomes larger, the curve tends to have more oscillations due to the wave reflection in the specimen with a finite size. However, the trends under different velocities are the same and fit with the experimental curve. Hence, we choose $v = 5\text{m/s}$ and $E_T = 1,150 \text{ MPa}$ for simulating the ductile fracture in the SNL challenge, as discussed next.

3.2 Ductile fracture prediction

The combined elastoplasticity and decohesion model, as described above, is used to predict the crack growth in the specimen as specified in the SNL challenge.

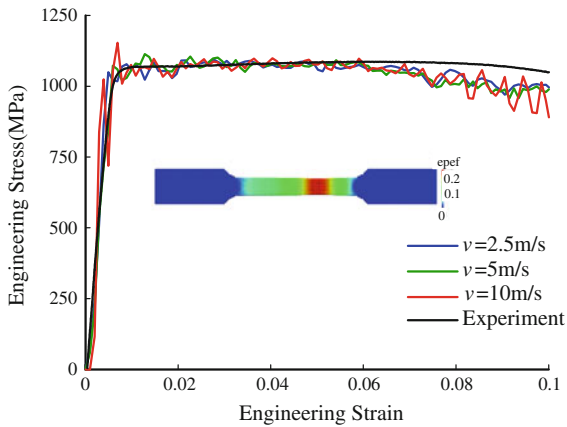


Fig. 2 The engineering stress–strain curves for tensile coupons (epcf denotes equivalent plastic strain)

Mode I only and Mode II only were considered as the dominant failure mode, respectively, in the decohesion model before becoming aware of the experimental data. However, the results with Mode I only were used for the blind prediction with the consideration that local mode I failure might be dominant in the evolution of failure. It has been found from recalibration that the failure mode would change due to the nonlocal nature of failure evolution, as discussed next.

The specimen geometry is illustrated in Fig. 6 and 8 of the lead article. The multi-level-grid MPM (Yang 2013) is used in the simulation, as depicted in

Fig. 3. Around the holes and cracking path, level 1 (small) background cells and the corresponding particles are used. In another region, level 0 (large) cells and corresponding particles are used. The cubic cell sizes in levels 1 and 0 are 0.125 and 0.25 mm, respectively. The number of particles in each cell is 8. Based on the calibration against available experimental data and for the purpose of simplicity, the decohesion parameters are chosen to be $\bar{u}_0 = 2 \times 10^{-7} \text{m}$ and $q = 1$, and the tensile and shear strengths are $s_{\text{max}} = 4,900 \text{MPa}$ and $\tau_{\text{max}} = 820 \text{MPa}$, respectively. The parameters s_{max} and τ_{max} are determined based on the C(T) specimen experiment results. A series of simulations with different values of s_{max} and τ_{max} have been performed, and the set of s_{max} and τ_{max} yielding the results closest to the experiment measurement is chosen as the final values of s_{max} and τ_{max} .

We first consider only one failure mode in the decohesion model. When only mode I is considered, we have $s_{\text{max}} = 4,900 \text{MPa}$, $\tau_{\text{max}} = \infty$ and $c_m = 100$; when only mode II is considered, we have $s_{\text{max}} = \infty$, $\tau_{\text{max}} = 820 \text{MPa}$ and $c_m = 0.01$. The cracking patterns under these two fracture modes are shown in Fig. 4a, b, and the corresponding force-COD curves are plotted in Fig. 5. When only mode I is considered, the crack develops from A to C, and finally arrives at E. The cracking path is perpendicular to the loading direction. The D1 specimen experiment also gives A-C-E crack path, and the force-COD curve is compared with that by the mode I

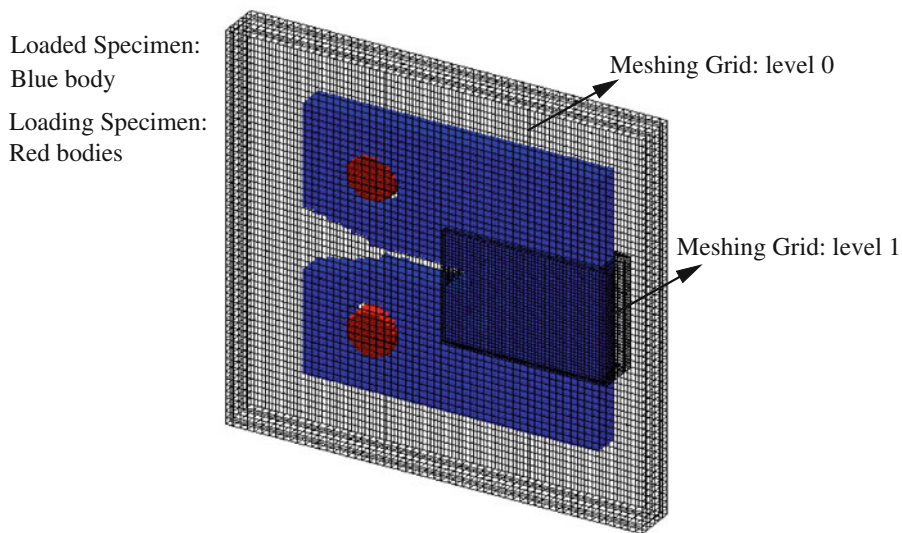


Fig. 3 The MPM computation model with a multi-level grid

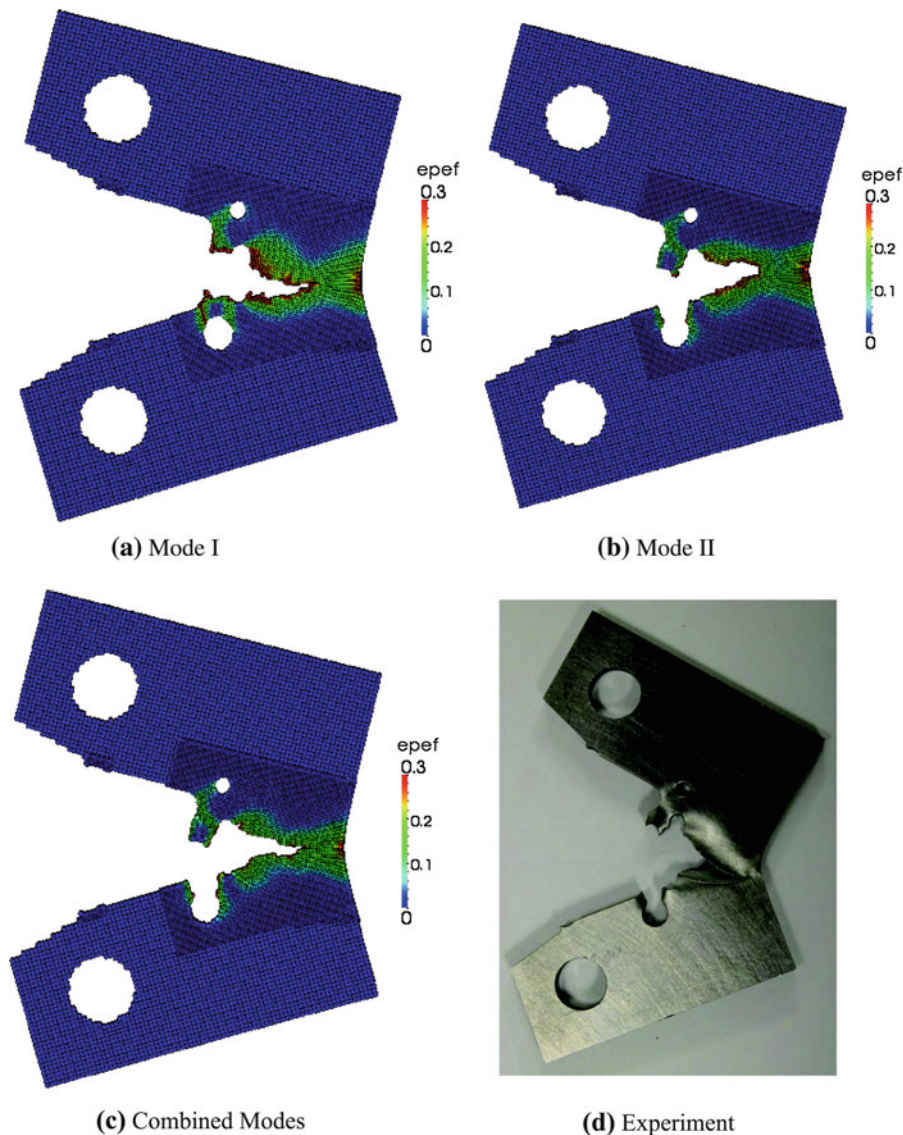


Fig. 4 Comparison of cracking patterns with different failure modes

simulation. As can be seen from Fig. 5, A to C crack path is formed much earlier in the results of mode I simulation. When only mode II is considered, the crack develops from A to D, then to C, and finally reaches E. But in the corresponding force-COD curve, there is no flat stage as the third crack is initiated.

Based on the above parametric study, it seems inappropriate to consider only one failure mode in the evolution of decohesion due to the nonlocal nature of failure evolution. Thus, we have considered mixed failure modes: when $s_1 > s_{\max}$ and $\tau_t > \tau_{\max}$, $c_m = 1$. The

resulting cracking pattern is shown in Fig. 4c, and the corresponding force-COD curve is plotted in Fig. 5, as compared with the experimental data. The crack first develops from hole A to D, and the crack path is along the loading direction which means the fracture mode is mainly mode II. Then the crack develops from hole D to C, and the crack path is also along the loading direction, which means that the fracture mode is mainly mode II. Finally, the crack develops from hole C to E, and the crack path is perpendicular to the loading direction, indicating that the fracture mode is mainly

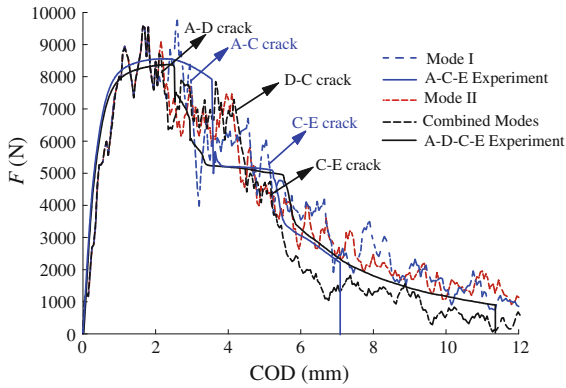


Fig. 5 Comparison of the force-COD curves with different failure modes

mode I. In the whole cracking process, three cracks are produced with each crack corresponding to the loading force drop on the force-COD curve. The detailed deformation patterns in the cracking process are demonstrated in Fig. 6. It is shown that both the cracking patterns and corresponding force-COD curve are consistent with the experimental data. Table 1 compares the simulation and experimental results, where F_{max} is the maximum loading force in the whole process, and C_1 , C_2 and C_3 denote the first, second and third crack initiation, respectively.

It should be pointed out that the values of the material parameters s_{max} and τ_{max} have a strong effect on the failure evolution. When $s_{max} = 3,000$ MPa and $\tau_{max} = 820$ MPa are chosen, the loading force is decreased to 1,000 N as the COD displacement reaches 3 mm, and the cracking pattern is similar to that in Fig. 4a for mode I fracture.

4 Concluding remarks

Both Mode I and Mode II failure were considered as the dominant failure mode, respectively, in the decohesion model before becoming aware of the SNL experimen-

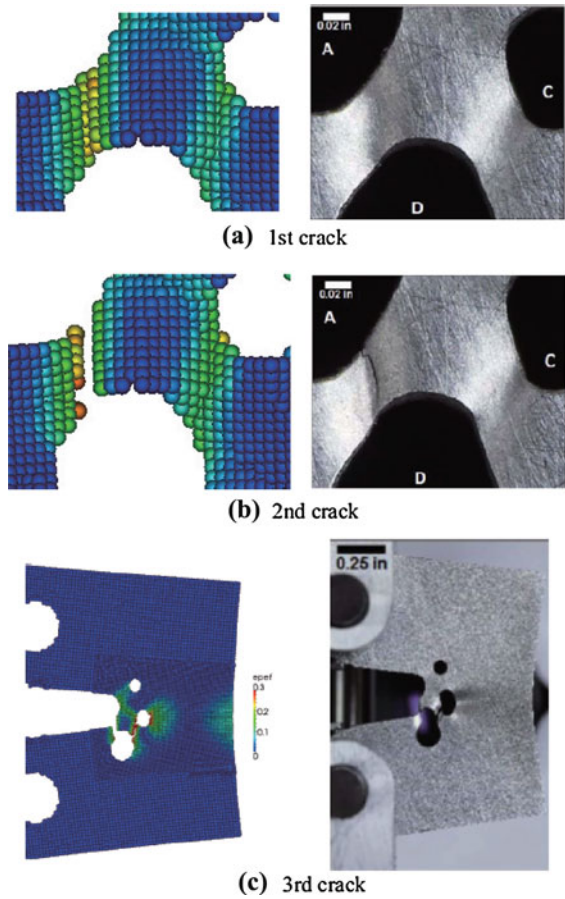


Fig. 6 The deformation patterns during the crack evolution

tal data, but the results with Mode I only were used for the blind prediction. Based on the parametric study and available experimental data, the proposed model-based simulation procedure has been calibrated to predict the essential feature of the observed cracking response. It is found that there is a transition between different failure modes along the cracking path, which depends on the stress distribution around the path because cracking is a nonlocal process. The MPM could effectively discretize the complex cracking path without additional

Table 1 Comparison between the simulation and experiment results

	F_{max} (N)	C_1		C_2		C_3		Crack path
		F (N)	d (mm)	F (N)	d (mm)	F (N)	d (mm)	
Simulation	9,553	8,734	2.10	6,963	4.00	4,748	5.15	A-D-C-E
Experiment	8,449	8,298	2.50	6,640	2.92	4,960	5.48	A-D-C-E

treatment. The high velocity boundary condition yields the response curve different from the quasi-static one, which might be due to the wave interactions associated with the high loading rate. However, the cracking pattern is not sensitive to the high loading rate. The numerical oscillation with the explicit MPM code appears to be large as compared with the experimental observation so the implicit MPM code might be an alternative choice. Since the simulation results for the post-peak response are sensitive to the decohesion parameters governing different kinds of failure modes, the image-based MPM should be developed to better predict the micromechanics involved in the failure evolution.

Acknowledgments This work was supported in part by the National Natural Science Foundation of China under Grant Number 11232003 and 11102185, and the National Key Basic Research Special Foundation of China under Grant Number 2010CB832701 and 2010CB832704.

References

- Bazant ZP, Chen EP (1997) Scaling of structural failure. *Appl Mech Rev* 50:593–627
- Belytschko T, Krongauz Y, Organ D, Fleming M, Krysl P (1996) Meshless methods: an overview and recent developments. *Comput Methods Appl Mech Eng* 139:3–48
- Chen Z (1996) Continuous and discontinuous failure modes. *J Eng Mech* 122:80–82
- Chen Z, Feng R, Xin X, Shen L (2003) A computational model for impact failure with shear-induced dilatancy. *Int J Numer Meth Eng* 56:1979–1997
- Chen Z, Gan Y, Chen JK (2008) A coupled thermo-mechanical model for simulating the material failure evolution due to localized heating. *CMES* 26:123–137
- Chen Z, Hu W, Shen L, Xin X, Brannon R (2002) An evaluation of the MPM for simulating dynamic failure with damage diffusion. *Eng Fract Mech* 69:1873–1890
- Chen Z, Shen L, Mai YW, Shen YG (2005) A bifurcation-based decohesion model for simulating the transition from localization to decohesion with the MPM. *ZAMP* 56:908–930
- Chen Z, Sulsky D (1995) A partitioned-modeling approach with moving jump conditions for localization. *Int J Solids Struct* 32:1893–1905
- Hu W, Chen Z (2006) Model-based simulation of the synergistic effects of blast and fragmentation on a concrete wall using the MPM. *Int J Impact Eng* 32:2066–2096
- Huang P, Zhang X, Ma S, Huang X (2011) Contact algorithms for the material point method in impact and penetration simulation. *Int J Numer Meth Eng* 85:498–517
- Ma Z, Zhang X, Huang P (2010) An object-oriented MPM framework for simulation of large deformation and contact of numerous grains. *CMES* 55:61–87
- Nairn JA (2003) Material point method calculations with explicit cracks. *CMES* 4:649–663
- Shen L, Chen Z (2005) A silent boundary scheme with the material point method for dynamic analyses. *CMES* 7:305–320
- Silling SA (2000) Reformulation of elasticity theory for discontinuities and long-range forces. *JMPS* 48:175–209
- Silling SA, Zimmermann M, Abeyaratne R (2003) Deformation of a peridynamic bar. *J Elast* 73:173–190
- Silling SA, Askari E (2005) A meshfree method based on the peridynamic model of solid mechanics. *Comput Struct* 83:1526–1535
- Sulsky D, Chen Z, Schreyer HL (1994) A particle method for history-dependent materials. *Comput Methods Appl Mech Eng* 118:179–196
- Yang P (2013) Material point method for localized failure problems. PhD thesis, Tsinghua University
- Yang P, Liu Y, Zhang X, Zhou X, Zhao Y (2012) Simulation of fragmentation with material point method based on Gurson model and random failure. *CMES* 85:207–236
- Zhang HW, Wang KP, Chen Z (2009) Material point method for dynamic analysis of saturated porous media under external contact/impact of solid bodies. *Comput Methods Appl Mech Eng* 198:1456–1472